Materials Research Bulletin 46 (2011) 1211–1218

Contents lists available at ScienceDirect

Materials Research Bulletin

journal homepage: www.elsevier.com/locate/matresbu

Hematite solid and hollow spindles: Selective synthesis and application in gas sensor and photocatalysis

Jiarui Huang [a,b,*], Min Yang [a], Cuiping Gu [a], Muheng Zhai [a], Yufeng Sun [c], Jinhuai Liu [b]

[a] College of Chemistry and Materials Science, Anhui Key Laboratory of Functional Molecular Solids, Anhui Normal University, 1# Beijing East Road, Wuhu 241000, PR China
[b] Research Center for Biomimetic Functional Materials and Sensing Devices, Institute of Intelligent Machines, Chinese Academy of Sciences, Hefei 230031, PR China
[c] Mechanical Engineering Department, Anhui Polytechnic University, Wuhu 241000, PR China

ARTICLE INFO

Article history:
Received 4 October 2010
Received in revised form 10 April 2011
Accepted 11 April 2011
Available online 16 April 2011

Keywords:
A. Microporous materials
A. Nanostructures
A. Semiconductors
B. Chemical synthesis

ABSTRACT

Hematite solid spindles and hollow spindles have been selectively synthesized by a template-free, economical hydrothermal method, using $FeCl_3{\cdot}6H_2O$ as the starting materials and NaOH as the homogeneous precipitant. XRD analyses indicated that the products consisted of α-Fe_2O_3. SEM and TEM measurements showed that the morphologies of products were in the shape of solid spindles and hollow spindles, respectively. A possible formation process based on the nucleation-oriented aggregation–recrystallization mechanism is proposed. Moreover, the as-prepared hollow spindle-like α-Fe_2O_3 exhibits a good response and reversibility to some organic gas, such as 2-propanol and acetone. Compared with other hematite nanostructures, the porous hollow hematite spindles show outstanding performance in gas sensing due to their large surface area and porous hollow structure. Because of the unique porous hollow structures of the samples, the photocatalytic property of the spindle-like α-Fe_2O_3 was also investigated.

1. Introduction

Currently, there is growing interest in the fabrication of nanostructures with desired morphologies and properties. Among the various morphologies of nanostructures, nanostructured hollow spheres are drawing intense research interest not only for their unique properties, but also for their broad range of applications such as in efficient catalysts, drug-delivery carriers, photonic crystals, energy-storage devices, optoelectronic sensors, and gas sensors [1–6].

Generally, manipulation of hollow materials is performed by template directed synthesis. Representative examples are the layer-by-layer deposition of nanoparticles onto spherical colloids (e.g., polystyrene beads and silica sol) [7–9] and sacrificial substitutions of metal nanoparticles by those with a higher standard reduction potential [10,11]. Following these procedures, the templates of colloidal spheres are removed via a timeconsuming treatment (e.g., calcination or dissolution with solvent) to form hollow structure. Template methods have proven to be effective and versatile for the synthesis of a wide array of hollow structures. Nonetheless, disadvantages related to tedious synthetic procedures and low yields have impeded the scale-up production and large-scale applications. In a sense, one-pot template-free synthesis is desirable and preferred. It will be a main task to explore other wet chemical means, aiming at a simple "one-pot" synthetic approach for hollow structures. So, the utilization of some physical phenomena, such as the Kirkendall effect or Ostwald ripening, provides new opportunities for the template-free fabrication of hollow spheres [12–14].

Among various inorganic materials, hematite (α-Fe_2O_3), a semiconductor with the band gap of 2.2 eV, is widely used in catalysts [15], pigments [16], sensors [17–19] and as the raw material for the synthesis of magnetic γ-Fe_2O_3. In addition to conventional applications, hollow hematite particles might also be used for encapsulation of various guest molecules, and this is likely to lead to novel applications in areas such as functional materials and medicine carrier. Among these fields, much of the interest has been focused on its application in gas sensor and photocatalysis, which will be greatly improved by the hollow structures of the particles [20–24]. Recently, many groups have synthesized Fe_2O_3 hollow structures through various methods. Chen and co-workers described a facile route for preparation of submicrometer ferrite/block copolymer hollow spheres [25]. Fe_2O_3 with ordered mesoporous structure and crystalline walls, was synthesized by use of mesoporous silica as template [26]. Upon calcination, Thomas and co-workers used carbohydrates and metal salts as reaction resources to synthesize various metal oxides sphere [27]. Because of the tedious work in the post treatment of the template,

* Corresponding author at: College of Chemistry and Materials Science, Anhui Key Laboratory of Functional Molecular Solids, Anhui Normal University, 1# Beijing East Road, Wuhu 241000, PR China. Tel.: +86 553 3869 303; fax: +86 553 3869 303.
E-mail address: jrhuang@mail.anhu.edu.cn (J. Huang).

0025-5408/$ – see front matter © 2011 Elsevier Ltd. All rights reserved.
doi:10.1016/j.materresbull.2011.04.004

solvothermal and hydrothermal methods were also employed in the preparation of the hollow nanostructures. For example, by a surfactant-assisted solvothermal method, submicrometer-sized hollow hematite particles were successfully prepared [28,29]. Using dimethylbenzene as solvent, Chen and co-workers had also succeeded in preparing the hematite hollow spindles [30]. Recently, the synthesis of hematite hollow spheres was also reported using by a hydrothermal method that employed surfactant such as cetyltriethylammnonium bromide (CTAB), oxalic acid and poly(ethylene glycol) [16,31,32]. However, it still remains a challenge for the selective synthesis among different hollow nanostructures by simply changing one experimental parameter, especially in a facile and environmental friendly way.

Herein we report a simple hydrothermal approach for selective synthesis of porous hollow and solid spindle-like α-Fe_2O_3 architectures, which require neither complicated techniques nor templates, and the effect of the surfactant CTAB was investigated to understand the formation mechanism of the hematite spindles. Furthermore, the photocatalysis and gas-sensing properties of the spindle-like α-Fe_2O_3 architectures are also discussed. The abstained nanoporous hollow spindle-like α-Fe_2O_3 architectures exhibit an excellent gas-sensing sensor signal with test gases.

2. Experimental details

2.1. Synthesis of the samples

To prepare the hematite solid spindles, 2 mmol $FeCl_3{\cdot}6H_2O$ was dissolved into 40 ml of deionized water under magnetic stirring. The pH of the solution was adjusted to 3.5 with 1 M NaOH solution. The resulting slurry was then transferred to a 50-ml Teflon-lined autoclave and maintained at 200 °C for 12 h. The autoclave was then cooled down to room temperature naturally. The final red solid products were centrifuged and washed with distilled water and absolute ethanol several times to ensure total removal of the inorganic ions and then dried at 60 °C under vacuum for 4 h. To prepare the hematite hollow spindles, with all the experiment parameters unchanged, and 219 mg CTAB, was added into the solution before adding NaOH solution.

2.2. Characterization

The products were characterized by X-ray diffraction (XRD, Shimadzu XRD-6000, with high-intensity Cu Kα radiation, wavelength 1.54178 Å), field emission scanning electron microscopy (FE-SEM, Hitachi S-4800, operated at 5 kV), high-resolution transmission electron microscopy (HRTEM, JEOL-2010 TEM with an acceleration voltage of 200 kV), and Brunauer–Emmett–Teller (BET) nitrogen adsorption–desorption (Nova 2000E). The pore-size distribution was determined from the adsorption branch of the isotherms using the Barett–Joyner–Halenda method.

2.3. Gas sensor fabrication and response test

The structures of the sensor device and the measurement system are the same as in our previous report [33]. The as-prepared spindle-like α-Fe_2O_3 nanostructures were directly coated on the outer surface of an alumina tube-like substrate on which a pair of Au electrodes had been printed previously, followed by drying at 60 °C for about 2 h and subsequent annealing at 360 °C for about 2 h. Finally, a small Ni-Cr alloy coil was inserted into the tube as a heater, which provided the working temperature of the gas sensor. In order to improve the long-term stability, the sensors were kept at the working temperature (280 °C) for 2 days. A stationary state gas distribution method was used for testing gas response in dry air. Detecting gases, such as ethanol vapor, were injected into a test chamber and mixed with air. The gas response of the sensor in this paper was defined as $S = R_a/R_g$ (reducing gases), where R_a is the resistance in dry air and R_g is that in the dry air mixed with detected gases. In our measurement system, the gas response of the sensor also can be calculated by the following equation:

$$S = \frac{V_{gas} \cdot (5000\,\mathrm{mV} - V_{air})}{V_{air} \cdot (5000\,\mathrm{mV} - V_{gas})},$$

where V_{air} and V_{gas} were the output voltages in air and test gas, respectively. The response or recovery time was expressed as the time taken for the sensor output to reach 90% of its saturation after applying or switching off the gas in a step function.

2.4. Photocatalysis measurement

The catalytic degradation of organic dyes was measured at room temperature under the irradiation of the 365 nm UV light for desired time. Hematite spindles (20 mg) were dispersed into 50 ml Rhodamine B aqueous solution of 10 mg/l. The optical property changes of dyes are recorded on a Hitachi U-3010 UV–vis absorption spectrophotometer (Tokyo, Japan), the above experiments were repeated using hematite hollow spindles under the same experimental conditions.

3. Results and discussion

3.1. Structure and morphology

Fig. 1 shows XRD patterns of the as-prepared Fe_2O_3 products. All the diffraction peaks were readily indexed to a pure rhombohedral phase of α-Fe_2O_3 (JSPDS card no. 89-2810). No other impurities could be detected by XRD. FE-SEM and TEM were employed to investigate the morphologies of the products. Fig. 2 displays the SEM and TEM images of the products. It can be seen that α-Fe_2O_3 product obtained when CTAB is absent are solid spindle-like structure as shown in Fig. 2a and b. Fig. 2c and d is the typical SEM and TEM images of the product obtained when CTAB is added, which shows that the product is composed of hollow spindles. The average size of the α-Fe_2O_3 spindles is approximately 2.5 μm along its major axis and approximately 1.6 μm along its minor axis, and the length-to-diameter ratio is about 1.6. Further observation of the α-Fe_2O_3 spindles showed that the surfaces of the spindles are rough. A careful observation of the surfaces of the hollow spindle-like α-Fe_2O_3 (inset of Fig. 2c) shows that the hollow spindle-like α-Fe_2O_3 is composed of many small nanoparticles. The magnified view (inset of Fig. 2c) indicates that their

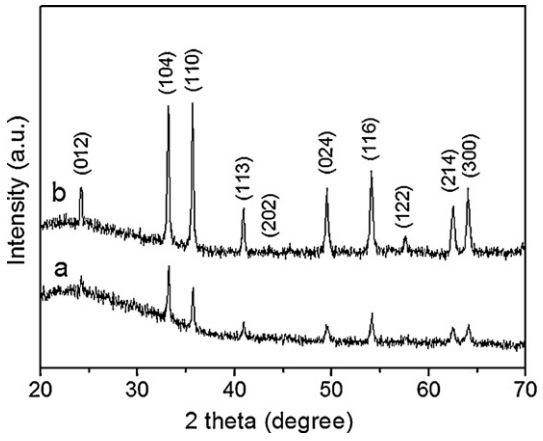

Fig. 1. XRD patterns of (a) α-Fe_2O_3 hollow spindles and (b) α-Fe_2O_3 solid spindles.

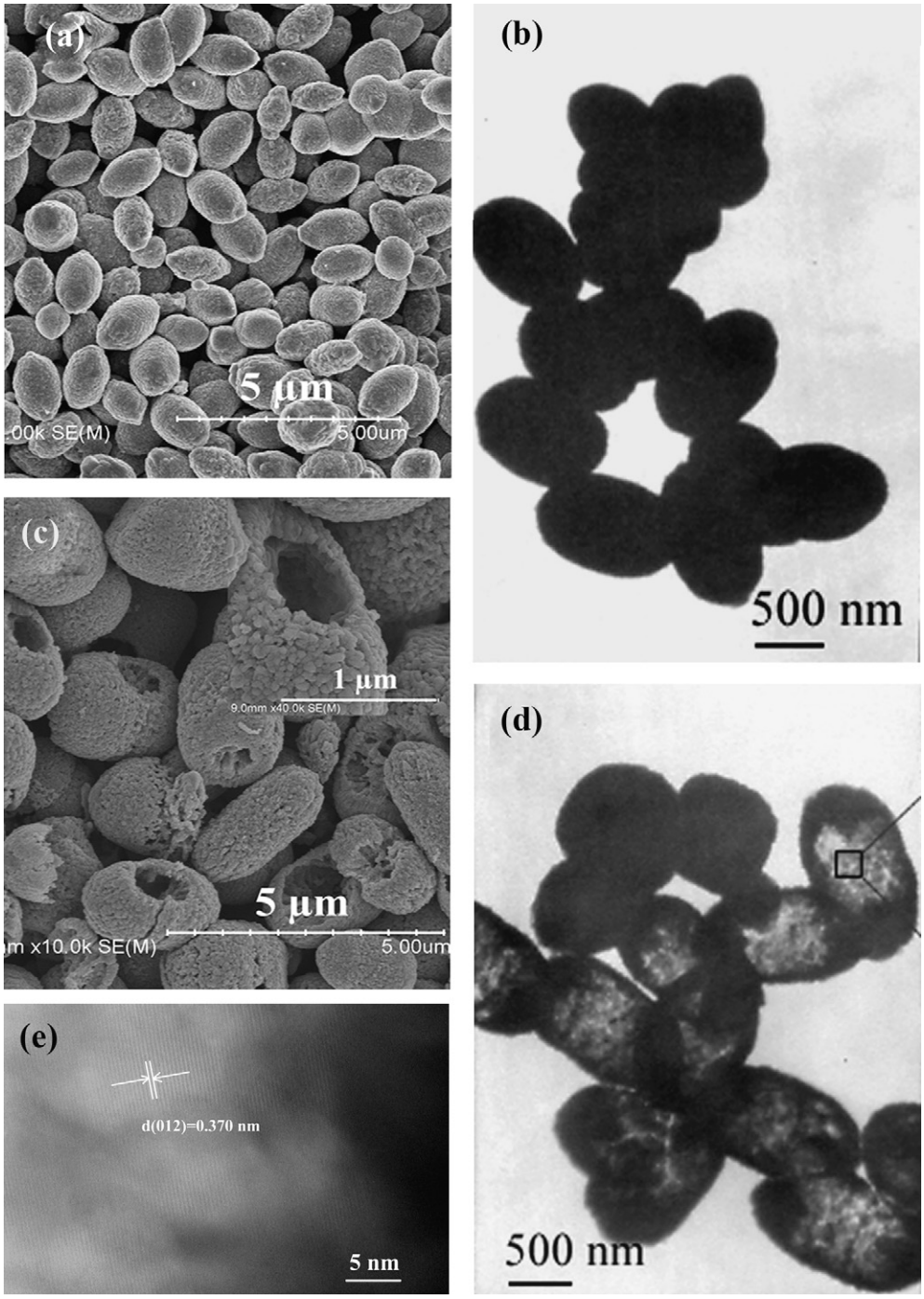

Fig. 2. (a) SEM and (b) TEM images of the α-Fe_2O_3 spindles obtained after hydrothermal reaction at 200 °C for 12 h when CTAB is absent; (c) SEM, (d) TEM, and (e) HRTEM images of the α-Fe_2O_3 porous hollow spindles obtained after hydrothermal reaction at 200 °C for 12 h when 0.218 g CTAB was added.

outer shell thickness is approximately 100 nm. High-resolution TEM image of the hollow spindle-like α-Fe_2O_3 (Fig. 2e taken from the part of Fig. 2d in rectangular frame) discloses clear lattice fringes with a spacing of 0.370 nm, which is consistent with the d value of the (0 1 2) plane [34].

To further confirm the inner architectures of the porous hollow α-Fe_2O_3 spindles, nitrogen adsorption and desorption measurements were performed to estimate the texture properties. The nitrogen adsorption and desorption isotherm and pore size distribution curve (inset) of porous hollow α-Fe_2O_3 spindles is shown in Fig. 3. The isotherm of the porous hollow α-Fe_2O_3 spindles sample exhibits a hysteresis loop at the p/p_0 ranges of 0.45–0.95, which is associated with the filling and emptying of mesopore by capillary condensation. This clearly indicates that the porous hollow α-Fe_2O_3 spindles sample exhibits a large textural porosity. Furthermore, the capillary condensation step is very sharp, which indicates a narrow distribution of mesopore size. The pore size distribution of the porous hollow α-Fe_2O_3 spindles sample shows that a narrow peak appeared in pore size region of 1.8–2.4 nm. The BET surface area of the hierarchically porous hollow α-Fe_2O_3 spindles was calculated to be 6.98 $m^2\ g^{-1}$, which is much higher than the surface area of the as-prepared solid Fe_2O_3 spindles (0.58 $m^2\ g^{-1}$).

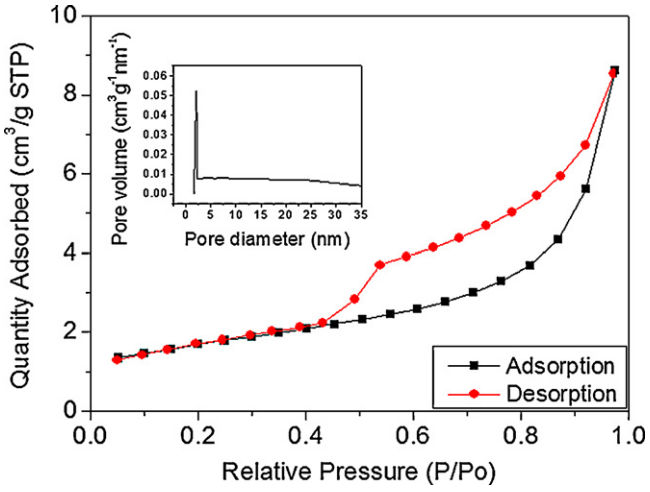

Fig. 3. Typical nitrogen adsorption–desorption isotherm and pore size distribution plots (inset) of the α-Fe_2O_3 porous hollow spindles.

3.2. Growth mechanism of the hollow structures

To investigate the growth mechanisms of such hollow nanostructures, time-dependent experiments were also carried out to clarify the formation mechanism. It is noteworthy that only solid Fe_2O_3 spindles were obtained (Fig. 4a and b) even after reacting at 200 °C for 1 h. When the reaction time was increased to 3 h, the solid Fe_2O_3 spindles turned into quasi-hollow Fe_2O_3 spindles (Fig. 4c and d) composed of nanoparticles were produced. As the reaction went on to a longer time (e.g., 9 h), the product was mainly composed of hollow Fe_2O_3 spindles (Fig. 4e and f). However, when the reaction time was increased to 15 h, the hollow Fe_2O_3 spindles turned broken (Fig. 4g and h). Based on the above SEM and TEM results, we proposed that the formation of hollow spindles was a simplified self-assembling process, which can be understood as a result of a nucleation-oriented aggregation–recrystallization mechanism from primary nanocrystals under high-temperature solvothermal conditions [35]. The formation of the hollow Fe_2O_3 spindles is schematically depicted in Fig. 5. In simple terms, primary hematite nanocrystals firstly nucleate in a supersaturated solution, resulting from the solvent-mediated hydrolysis of Fe^{3+}. The freshly formed nanocrystals are unstable due to their high surface energy, and thus have a great tendency to spontaneously aggregate. During the aggregation process, the adjacent primary nanocrystals align in an orderly way by an oriented-attachment mechanism so that the particles share a planar interface in a common crystallographic orientation [36]. Firstly, the CTAB ions coordinate with the surface Fe atoms of precursor preferentially and lead to the formation of the solid spindles. During the hydrothermal process, the nanoparticles comprising the solid spindles decomposed and recrystallized. The dissolution primarily occurred in the spindles' interior because of the high surface energy of the nanocrystals, while the exterior shells have the relative lower surface energy because of the stabilization of oxalate ions. Thus, hollow spindles formed. But the hollow spindles were broken for the decomposition and recrystallization process lasting too long. To further prove the formation mechanism of the hollow spindles, the reaction was also carried out at 100 °C for 12 h, in which only small amounts of solid spindles and nanorods formed. The reason why no hollow spindles obtained may be due to the higher temperature required for the dissolution and recrystallization.

3.3. Gas-sensing properties of the α-Fe_2O_3 spindles

Hierarchical or porous semiconductor metal oxides are promising materials for gas sensor. Their special structures can usually provide a large surface-to-volume ratio, which is most favorable for the diffusion of target gases in sensor materials. Many studies have proven that these special structures could significantly enhance the sensor performance. In addition, the high porosity of the as-prepared hierarchically porous architectures provides excellent channels and "surface accessibility" for the mass transportation of target gases. Because of these advantages that are not available from bulk or solid materials, the as-prepared hierarchically porous nanostructures are expected to exhibit excellent properties for gas sensor applications.

The gas sensors are fabricated from the as-prepared porous hollow Fe_2O_3 spindles and solid Fe_2O_3 spindles for comparison. Fig. 6a–d shows the real-time response curve and the sensor responses of the porous hollow Fe_2O_3 spindle sensor upon exposure to different concentrations of ethanol, acetone, 2-propanol and n-butanol at a working temperature of 280 °C, respectively. The as-prepared porous hollow Fe_2O_3 spindles have a good response to these kinds of organic vapors. At a low concentration of 1 ppm of ethanol, acetone, 2-propanol and n-butanol, the relative responses are about 2.7, 1.5, 2.4 and 1.7, respectively. At a high concentration of 100 ppm of ethanol, acetone, 2-propanol and n-butanol, the relative responses are about 17.4, 21.5, 23.0 and 13.9, respectively. Furthermore, according to Fig. 6, we could observe that the sensor also had a good reversibility. In the same measurement system, the as-prepared solid Fe_2O_3 spindles also have responses to ethanol, acetone, 2-propanol and n-butanol. However, the response of solid Fe_2O_3 spindles to 100 ppm ethanol, acetone, 2-propanol and n-butanol are 4.3, 5.8, 4.1 and 6.2, respectively, which are much lower than those of the porous hollow Fe_2O_3 spindles as shown in Fig. 7. Furthermore, the response of the porous hollow Fe_2O_3 spindles to ethanol is much higher than those of Fe_2O_3 hollow sea urchins [20], nanocubes [20], mesoporous hollow spheres [37], and porous nanospheres [38].

When increasing ethanol concentration, the response of the sensor also sharply increased, as shown in Fig. 6a. The response to 200 ppm ethanol is up to 32.8, and the response time and recovery time were about 3 s and 14 s, respectively. It is obvious that the gas sensor exhibits rapid gas-sensing behaviors when the target gases are injected or released. This can be explained from the aspect of gas diffusion. Assuming Knudsen flow, the diffusion coefficient of the target gases can be defined by Eq. (1) [39].

$$D_K = \frac{\varepsilon d}{3\tau}\left(\frac{8RT}{\pi M}\right)^{1/2} \quad (1)$$

where D_K is the Knudsen diffusion coefficient in a porous medium; ε, τ, d, R, T, and M are dimensionless porosity, dimensionless tortuosity, pore diameter, gas constant, temperature, and molar mass, respectively. From the equation presented above, the gas diffusion is directly proportional to the porosity and pore diameter, while it is inversely proportional to the pore tortuosity. BET analysis has revealed an average pore diameter of the porous hollow Fe_2O_3 spindles of about 2.1 nm. Besides, the hollow structure also has been investigated by observations of the morphology of Fe_2O_3 spindles. The tortuous pore network between Fe_2O_3 spindles in the sensitivity film also improves the gas diffusion. Therefore, the porous hollow Fe_2O_3 spindle film is suggested to allow fast diffusion of gas molecules, resulting in the high rates of gas adsorption and desorption. This could be considered as a contributor to the highly sensitive performance of the as-fabricated gas sensor. So, the porous hollow Fe_2O_3 spindles are observed to demonstrate good sensitivity to the organic vapors. At the same time, an additional two sensors were fabricated under the same process. Similar gas-sensing properties

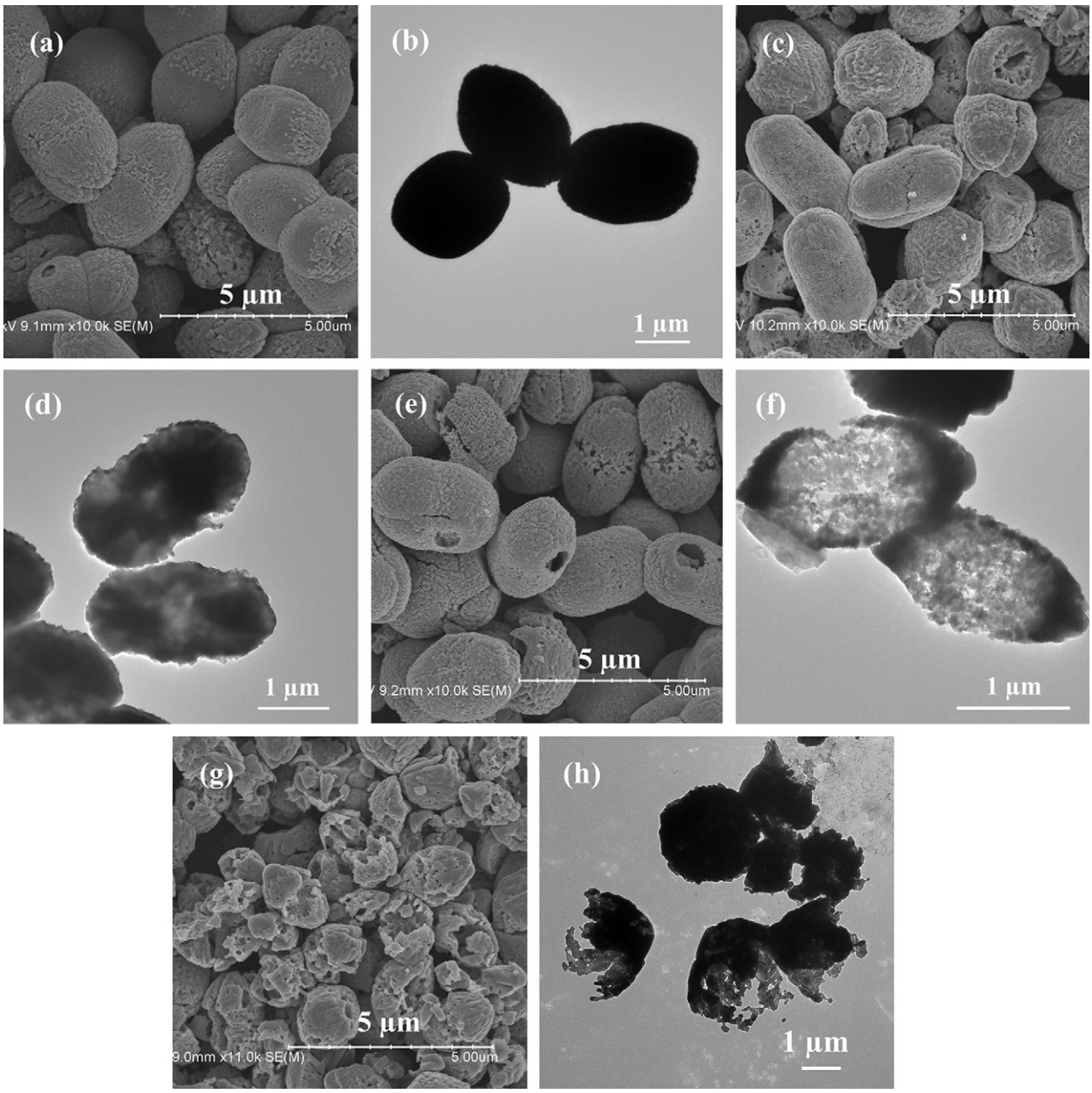

Fig. 4. SEM and TEM images of the α-Fe_2O_3 spindles obtained after hydrothermal reaction at 200 °C for (a, b) 1 h, (c, d) 3 h, (e, f) 9 h, and (g, h) 15 h at the presence of 0.218 g CTAB.

were obtained, which suggests the good repeatability of the sensors.

For the semiconductor oxide sensors, working temperature is an important factor. Fig. 8 presents the relationship between the sensor responses and the working temperature. In the range of 220–320 °C, the sensor response to ethanol was sharply increased with increasing working temperature, and up to 17.4 at 280 °C. Then, the sensor response was decreased at higher working temperature. So, the optimum working temperature of the sensor device was 280 °C.

3.4. The property of photocatalytic degradation for organic dyes

To evaluate the photocatalytic activity of our products, we measured the optical property changes of Rhodamine B aqueous solution in the presence of hematite solid spindles or hematite hollow spindles under the irradiation of the 365 nm UV light for given time, respectively. The time-dependent absorption spectra of Rhodamine B solution containing α-Fe_2O_3 architectures catalyst during the irradiation are illustrated in Fig. 9. It can be seen that the maximum absorbance at 552 nm decreased rapidly with irradiation time. The absorption intensity of the peak was reduced by about 14% when the solution has been irradiated under 360 nm UV light for 15 min in the presence of any hematite spindles. While after it had been irradiated under 360 nm UV light for 120 min, its absorption peak disappeared almost completely, indicating that most amount of Rhodamine B was degraded. The parallel experiment when hematite hollow spindles as the photocatalyst but in the dark have been carried out and the results were shown in Fig. 9c. As seen from Fig. 9c, the amount of Rhodamine B was almost not degraded due to the absence of the UV irradiation. The decoloration of solution may be due to the destruction of the dye

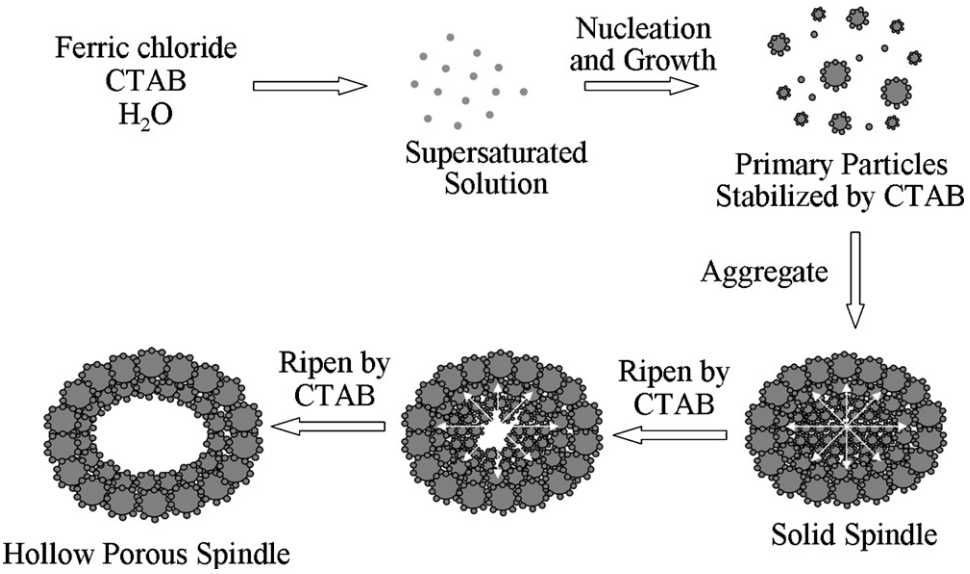

Fig. 5. The schematic illustration of the formation of α-Fe_2O_3 hollow spindles by means of a repeating reaction–dissolution mechanism.

chromogen. Since no new absorption peak was observed, the Rhodamine B has been decomposed. It is obvious that the hematite solid spindles and hematite hollow spindles were effective photocatalysts for the direct degradation of Rhodamine B. The fitting of absorbance maximum plot versus time indicates an exponential decay as shown in Fig. 9 (insert). The normalized concentration of the solution equals the normalized maximum absorbance, so we use C_0/C to take place of A_0/A, where C_0 and C are the initial and actual concentration of Rhodamine B, respectively. The photocatalytic properties in the degradation of Rhodamine B of the hematite spindles suggest that the products may have potential application in water treatment. It is generally accepted that the catalytic process is mainly related to the adsorption and desorption of molecules on the surface of the catalyst. The high specific surface area of the hematite porous hollow spindles results in more unsaturated surface coordination sites exposed to the solution. In addition, the hierarchical structures in the catalyst enable storage of more molecules. However, from Fig. 9a and b the as-obtained hematite hollow spindles do not obviously show more effective than the solid spindles. This is mainly for the shell of the

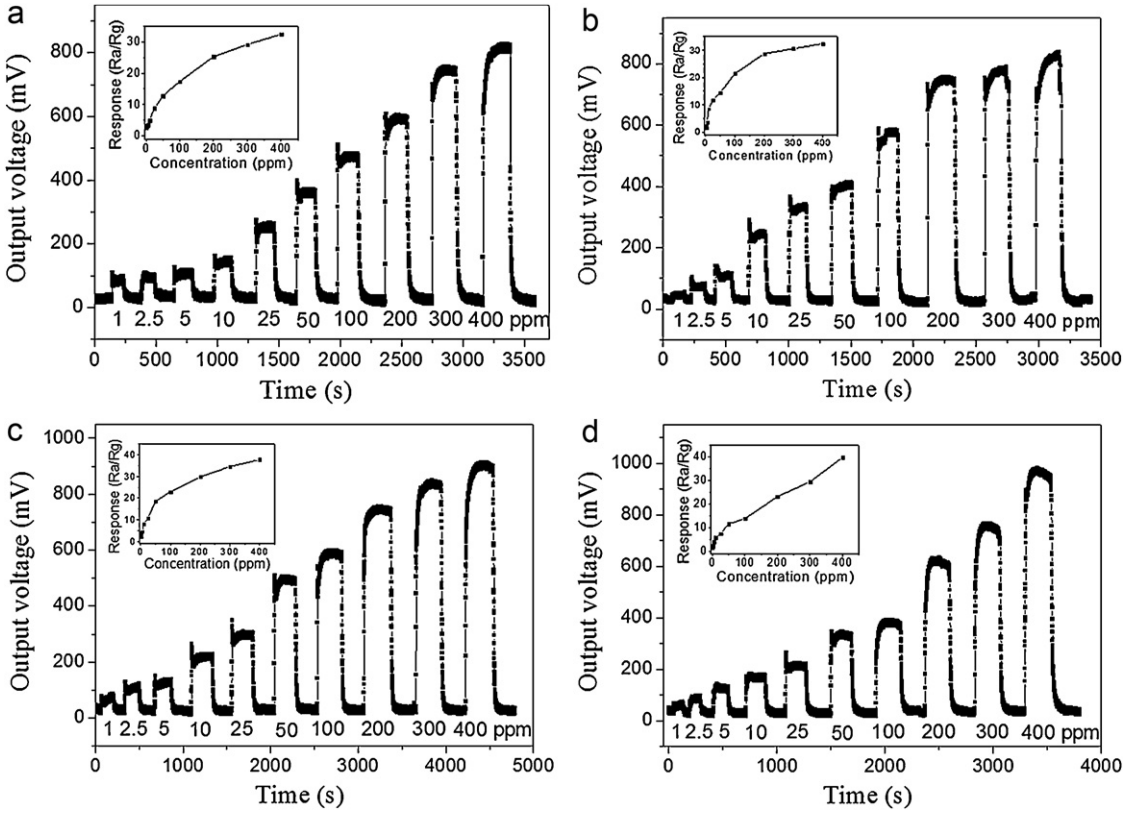

Fig. 6. Real-time response curves of the α-Fe_2O_3 porous hollow spindle sensor upon exposure to different concentrations of ethanol (a), acetone (b), 2-propanol (c), and n-butanol (d) at a working temperature of 280 °C. The insets show the corresponding sensor response curves.

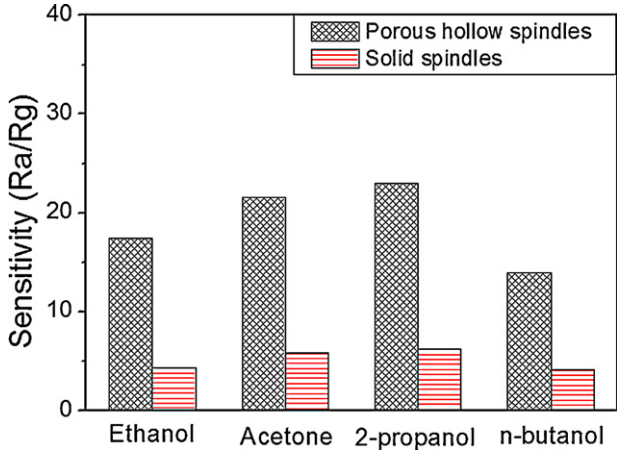

Fig. 7. Responses of the sensors based on two kinds of α-Fe_2O_3 spindles upon exposure to 100 ppm of ethanol, acetone, 2-propanol, and n-butanol at a working temperature of 280 °C.

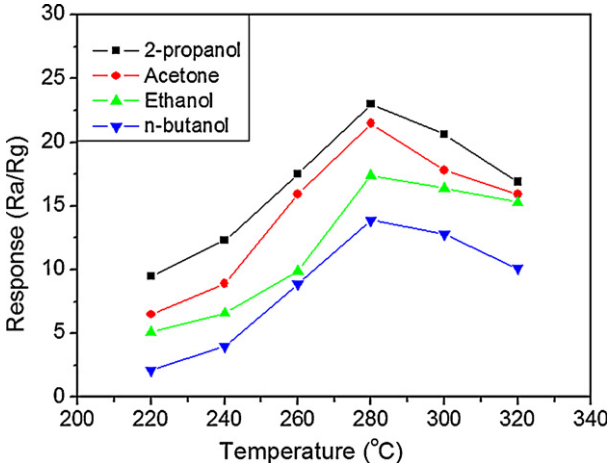

Fig. 8. Sensor responses of the α-Fe_2O_3 porous hollow spindle sensor upon exposure to 100 ppm of ethanol, 2-propanol, n-butanol, and acetone at different working temperatures.

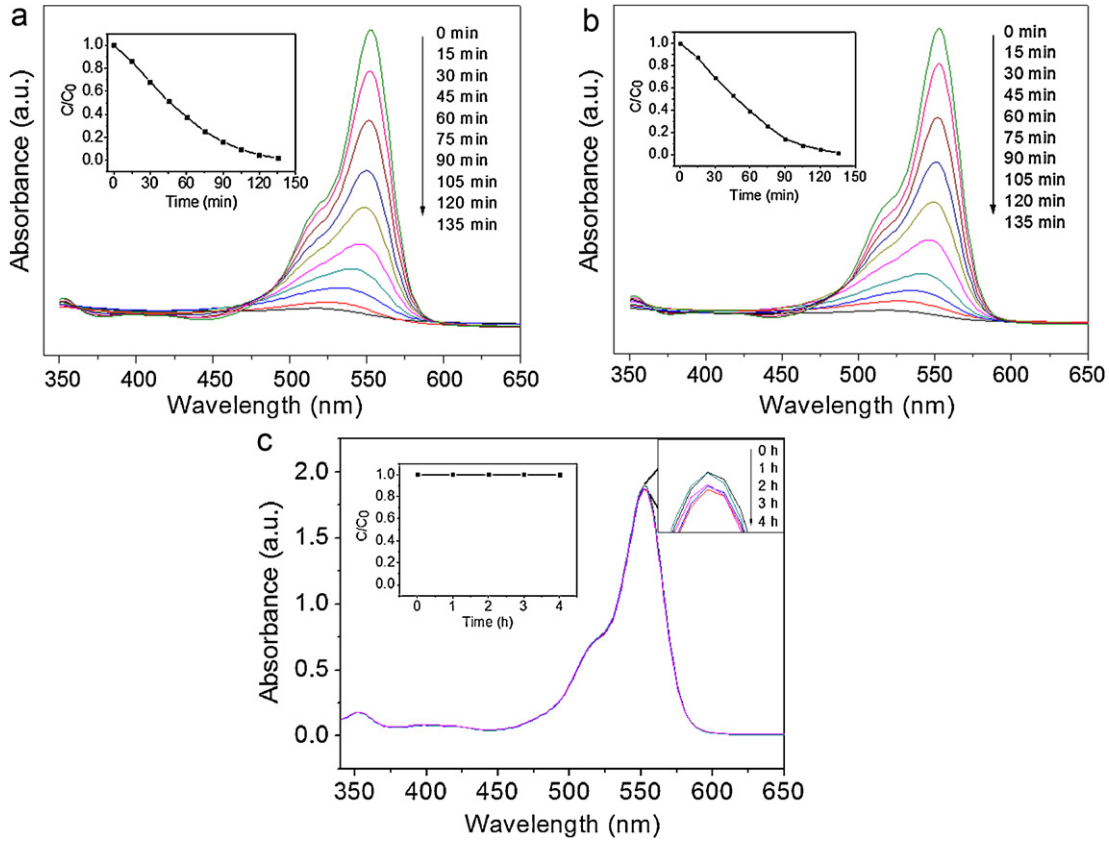

Fig. 9. Absorption spectrum of the Rhodamine B solution (10 mg/L, 20 mL) in the presence of (a) the α-Fe_2O_3 porous hollow spindles, (b) the α-Fe_2O_3 solid spindles under UV irradiation, and (c) the α-Fe_2O_3 porous hollow spindles in the dark. Photodegradation plots (insert) of Rhodamine B under UV-light, in which C is the concentration of Rhodamine B and C_0 is the initial concentration.

hematite hollow spindles is too thick and the UV light can not irradiate the inner surface area of the hematite hollow spindles, as a result, the inner surface area is disabled for photocatalytic degradation according to the parallel experiment result.

4. Conclusions

In summary, α-Fe_2O_3 solid spindles and hollow spindles with size of 2–3 μm were successfully synthesized by a convenient hydrothermal method. Gas sensors were fabricated from the as-synthesized α-Fe_2O_3 spindles and applied to detecting some reducing gases. Comparative gas sensing tests between gas sensors based on α-Fe_2O_3 hollow spindles and solid spindles clearly show that the former exhibits more excellent sensing performances, implying a good potential of the hollow porous α-Fe_2O_3 nanostructures for sensor applications. The enhanced sensing performances are attributed to the high porosity and 3D morphology, which can significantly facilitate gas diffusion and mass transportation in sensing materials. Furthermore, the as-prepared spindle-like α-Fe_2O_3 exhibits superior photocatalytic property on photocatalytic

decomposition of Rhodamine B. However, as for photocatalytic decomposition of Rhodamine B, the as-obtained hematite hollow spindles do not obviously show more effective than the solid spindles mainly due to the inner surface area being disabled for photocatalytic degradation.

Acknowledgements

This work has been supported by National Basic Research Program of China (973 Program 2007CB936602 and 2011CB933700), Young College Teachers' Research Fund Program of Anhui Normal University (Project Nos. 2009xqn70 and 2009xqn71), and Anhui Provincial Natural Science (Project Nos. 10040606Q34 and 090412036).

References

[1] F. Caruso, Chem. Eng. J. 6 (2000) 413.
[2] K. Kamata, Y. Lu, Y.N. Xia, J. Am. Chem. Soc. 125 (2003) 2384.
[3] C.E. Fowler, D. Khushalani, S. Mann, Chem. Commun. 19 (2001) 2028.
[4] Y. Wan, D.Y. Zhao, Chem. Rev. 107 (2007) 2821.
[5] L.F. He, Y. Jia, F.L. Meng, M.Q. Li, J.H. Liu, J. Mater. Sci. 44 (2009) 4326.
[6] J.H. Lee, Overview: Sens. Actuators B 140 (2009) 319.
[7] A.B. Bourlinos, M.A. Karakassides, D. Petridis, Chem. Commun. 16 (2001) 1518.
[8] S.W. Kim, M. Kim, W.Y. Lee, T. Hyeon, J. Am. Chem. Soc. 124 (2002) 7642.
[9] F.Y. Yang, Y. Chu, S.Y. Ma, Y.P. Zhang, J.L. Liu, J. Colloid Interface Sci. 301 (2006) 470.
[10] Y.G. Sun, Y.N. Xia, Science 298 (2002) 2176.
[11] Y.G. Sun, B. Mayers, Y.N. Xia, Adv. Mater. 15 (2003) 641.
[12] Y.D. Yin, R.M. Rioux, C.K. Erdonmez, S. Hughes, G.A. Somorjai, A.P. Alivisatos, Science 304 (2004) 711.
[13] Y. Chang, J.J. Teo, H.C. Zeng, Langmuir 21 (2005) 1074.
[14] L.L. Li, Y. Chu, Y. Liu, L.H. Dong, J. Phys. Chem. C 111 (2007) 2123.
[15] Y.H. Zheng, Y. Cheng, Y.S. Wang, F. Bao, L.H. Zhou, X.F. Wei, Y.Y. Zhang, Q. Zheng, J. Phys. Chem. B 110 (2006) 3093.
[16] K.J. Sreeram, R. Indumathy, A. Rajaram, B.U. Nair, T. Ramasami, Mater. Res. Bull. 41 (2006) 1875.
[17] C.Z. Wu, P. Yin, X. Zhu, C.Z. OuYang, Y. Xie, J. Phys. Chem. B 110 (2006) 17806.
[18] W. Zheng, Z.Y. Li, H.N. Zhang, W. Wang, Y. Wang, C. Wang, Mater. Res. Bull. 44 (2009) 1432.
[19] J. Chen, L.N. Xu, W.Y. Li, X.L. Gou, Adv. Mater. 17 (2005) 582.
[20] F.H. Zhang, H.Q. Yang, X.L. Xie, L. Li, L.H. Zhang, J. Yu, H. Zhao, B. Liu, Sens. Actuators B 141 (2009) 381.
[21] J.Y. Zhong, C.B. Cao, Sens. Actuators B 145 (2010) 651.
[22] X. Li, X. Yu, J.H. He, Z. Xu, J. Phys. Chem. C 113 (2009) 2837.
[23] S.W. Cao, Y.J. Zhu, J. Phys. Chem. C 112 (2008) 6253.
[24] X.L. Xie, H.Q. Yang, F.H. Zhang, L. Li, J.H. Ma, H. Jiao, J.Y. Zhang, J. Alloys Compd. 477 (2009) 90.
[25] X.H. Li, D.H. Zhang, J.S. Chen, J. Am. Chem. Soc. 128 (2006) 8382.
[26] F. Jiao, A. Harrison, J.C. Jumas, A.V. Chadwick, W. Kockelmann, P.G. Bruce, J. Am. Chem. Soc. 128 (2006) 5468.
[27] M.M. Titirici, M. Antonietti, A. Thomas, Chem. Mater. 18 (2006) 3808.
[28] D.H. Chen, D.R. Chen, X.L. Jiao, Y.T. Zhao, J. Mater. Chem. 13 (2003) 2266.
[29] S.Y. Lian, E.B. Wang, L. Gao, D. Wu, Y.L. Song, L. Xu, Mater. Res. Bull. 41 (2006) 1192.
[30] J. Lu, D.R. Chen, X.L. Jiao, J. Colloid Interface Sci. 303 (2006) 437.
[31] S.Y. Zeng, K.B. Tang, T.W. Li, Z.H. Liang, D. Wang, Y.K. Wang, W.W. Zhou, J. Phys. Chem. C 111 (2007) 10217.
[32] L.L. Li, Y. Chu, J. Nanosci. Nanotechnol. 10 (2010) 5282.
[33] J.R. Huang, Y.J. Wu, C.P. Gu, M.H. Zhai, K. Yu, M. Yang, J.H. Liu, Sens. Actuators B 146 (2010) 206.
[34] J.B. Lian, X.C. Duan, J.M. Ma, P. Peng, T. Kim, W.J. Zheng, ACS Nano 3 (2009) 3749.
[35] X.L. Hu, J.C. Yu, Adv. Funct. Mater. 18 (2008) 880.
[36] X.L. Fang, C. Chen, M.S. Jin, Q. Kuang, Z.X. Xie, S.Y. Xie, R.B. Huang, L.S. Zheng, J. Mater. Chem. 19 (2009) 6154.
[37] Z.C. Wu, K. Yu, S.D. Zhang, Y. Xie, J. Phys. Chem. C 112 (2008) 11307.
[38] H.M. Chen, Y.Q. Zhao, M.Q. Yang, J.H. He, P.K. Chu, J. Zhang, S.H. Wu, Anal. Chim. Acta 659 (2010) 266.
[39] J.W. Veldsink, R.M.J. Van Damme, G.F. Versteeg, W.P.M. Van Swaaij, Chem. Eng. J. Biochem. Eng. J. 57 (1995) 115.